



OPEN

# Plasmon-assisted radiolytic energy conversion in aqueous solutions

SUBJECT AREAS:  
ELECTRONIC PROPERTIES  
AND MATERIALS  
BATTERIES

Baek Hyun Kim &amp; Jae W. Kwon

Department of Electrical and Computer Engineering, University of Missouri, Columbia, MO 65211, United States.

Received  
28 March 2014Accepted  
14 May 2014Published  
11 June 2014Correspondence and  
requests for materials  
should be addressed to  
J.W.K. (kwonj@  
missouri.edu)

The field of conventional energy conversion using radioisotopes has almost exclusively focused on solid-state materials. Herein, we demonstrate that liquids can be an excellent media for effective energy conversion from radioisotopes. We also show that free radicals in liquid, which are continuously generated by beta radiation, can be utilized for electrical energy generation. Under beta radiation, surface plasmon obtained by the metallic nanoporous structures on TiO<sub>2</sub> enhanced the radiolytic conversion via the efficient energy transfer between plasmons and free radicals. This work introduces a new route for the development of next-generation power sources.

Articles emitted from radioisotopes can be used to convert the radiant energy into electricity. Radioisotope energy conversion for power generation has been intensively studied to develop power sources for wide range of applications, from energizing cardiac pacemakers in human body<sup>1</sup> to challenging outer planet missions<sup>2</sup>. As compared to various indirect conversion methods, which collect electricity from the secondary energy forms of heat or light generated by radiation<sup>3,4</sup>, direct conversion methods produce electric power straight from energetic particles<sup>5,6</sup>. Beta particles can produce electron-hole pairs in semiconductors via their loss of kinetic energy and can contribute to the generation of electric power<sup>6</sup>. Although potential applicability of radioisotopes in portable power sources that do not require recharging seems very attractive<sup>7</sup>, it has been reported that only a small portion of the entire radiation energy can be converted into electrical energy<sup>5–10</sup>. Moreover, most betavoltaic cells suffer from serious radiation damage to the lattice structures of semiconductors and subsequent performance degradation due to the high kinetic energy of the beta particles<sup>11</sup>. Alternatively, to minimise lattice damage in semiconductors, wide band gap materials are typically used. However, radiation-resistive materials, such as SiC and GaN, still show very low energy conversion efficiencies<sup>12,13</sup>. Little improvement has been made even after vigorous research on various improvement methods utilizing porous structures<sup>14</sup>, inverted pyramidal cavities<sup>15</sup>, and three dimensional silicon pillar structures<sup>15</sup> to increase rectifying junction areas. Although, thus far, there is no method for completely avoiding radiation damage to semiconductors, the use of a liquid-phase semiconductor material has been introduced as a possible means to overcome the radiation damage and structural defect problem<sup>16</sup>. One major benefit of utilising a liquid-phase material is the well-known ability to efficiently absorb the kinetic energy of beta particles<sup>17</sup>.

Since the advent of nuclear power, liquids have been intensively studied for use as a radiation-shielding material. Large amounts of radiation energy can be absorbed by water. When radiation energy is absorbed by an aqueous solution, free radicals (e.g.,  $e_{aq}^-$ ,  $\cdot\text{OH}$ ,  $\text{H}^\cdot$ ,  $\text{HO}_2^\cdot$ ) can be produced through radiolytic interactions<sup>18–20</sup>. These free radicals are known to affect the generation of molecular by-products, such as H<sub>2</sub>O<sub>2</sub> and H<sub>2</sub><sup>21–24</sup>. However, counterintuitively, the generation of electricity from a solution containing an ample amount of absorbed radiation energy has not yet been vigorously studied. Here, we demonstrate a new method for the generation of electricity using a device that separates the radiolytic current from the free radicals by splitting the water.

## Results

**Design and operating principle of Pt/nanoporous TiO<sub>2</sub> radiolytic cell.** Our water splitter is composed of a nanoporous semiconductor coated with a thin Pt film to produce a specially designed metal-semiconductor junction (Fig. 1a). As a suitable semiconductor material for water decomposition, we used a very stable and common large band gap oxide material, TiO<sub>2</sub>, because the use of large band gap oxide materials as a semiconducting catalyst can improve the radiolysis yield<sup>25–27</sup>. Nanoporous TiO<sub>2</sub> was formed by anodising and subsequently thermally oxidising a thin Ti film. The large surface area of the porous structure can provide more chemical reaction sites than a planar surface. To form a stable Schottky contact at the semiconductor/metal

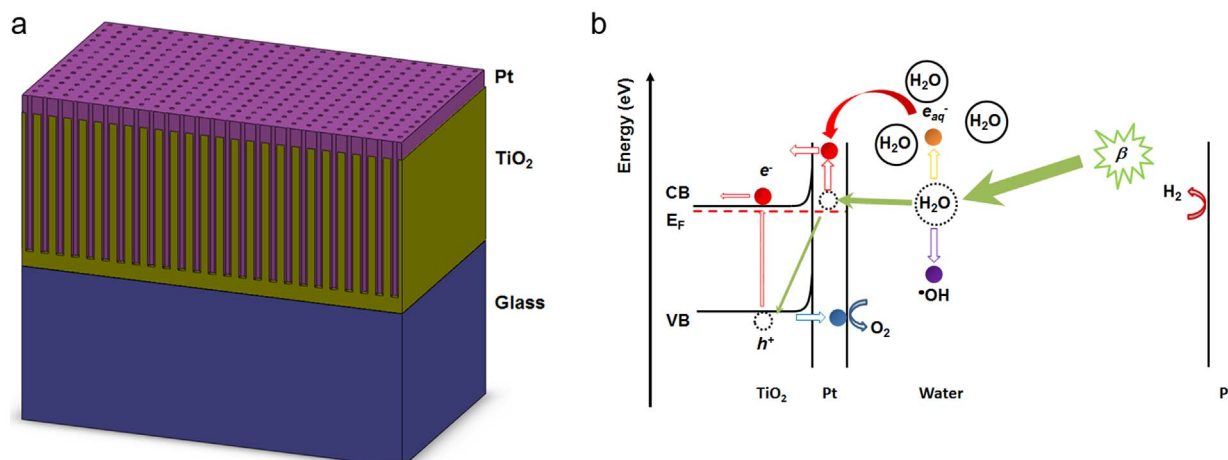


**Figure 1 | Structure and mechanism of the plasmon-assisted radiolytic water splitter.** (a), Cross-sectional schematic illustration of nanoporous  $\text{TiO}_2$  prepared by anodising and thermally oxidising a thin Ti film deposited on a glass substrate. The thin Pt film is deposited on top of the  $\text{TiO}_2$  nanopores using an RF sputtering system. (b), Energy level diagram of a surface-plasmon-assisted radiolytic water splitter. CB, conduction band; VB, valence band;  $E_F$ , Fermi energy;  $e_{aq}^-$ , aqueous electron;  $\cdot\text{OH}$ , hydroxyl free radical;  $\beta$ , beta radiation.

interface, a thin Pt film was uniformly deposited using a radio frequency (RF) sputtering system. As shown in the band diagram of the junctions in Fig. 1b, a Schottky barrier of 0.45 eV is formed because the Fermi energy ( $E_F$ ) of  $\text{TiO}_2$ , an n-type semiconducting oxide, is 5.2 eV<sup>28,29</sup> while that of Pt is 5.65 eV<sup>30</sup> with respect to the vacuum level. To experimentally confirm the Schottky barrier height between Pt and  $\text{TiO}_2$ , we performed XPS analysis and measured the Schottky barrier height of 0.6 eV between Pt and Pt/ $\text{TiO}_2$  layers. When high-energy beta radiation passes through Pt and nanoporous  $\text{TiO}_2$ , electron-hole pairs are produced inside the nanoporous  $\text{TiO}_2$ . In particular, the holes generated in  $\text{TiO}_2$  move toward the Pt/liquid interface and then react with redox couples of water molecules, while the electrons are transported through the nanoporous  $\text{TiO}_2$  to the other electric contact due to the built-in potential at the Pt/electrolyte interface. In general,  $\text{TiO}_2$  is resistant to corrosion, but the additional layer of Pt can further protect the  $\text{TiO}_2$  layer under the harsh conditions of high pH values that are needed for water splitting. In addition, the porosity of the  $\text{TiO}_2$  leads to myriad nanoholes in the Pt film, which create localised surface plasmons that act as harmonic oscillators in response to an oscillating external electric field. Since the first report<sup>31</sup> of the generation of surface plasmons on rough metal surfaces by electron illumination in 1977, many studies have examined various metal structures<sup>32–35</sup>. Surface plasmons excited on the Pt surface can produce electron-hole pairs, with the excited electrons transiently occupying normally empty states in the Pt conduction band above the Fermi energy level. Most of the excited electrons are sufficiently energetic to enter the conduction band of  $\text{TiO}_2$ .

In contrast to photocatalytic cells, high-energy beta radiation in our device can produce free radicals in water through the loss of kinetic energy. In a meta-stable state, the free radicals are recombined into water molecules or trapped in water molecules<sup>36–38</sup>. Thus, the free radicals produced by the radiation can be converted into electricity by a plasmon-assisted, wide band gap oxide semiconducting material using a water splitting technique at room temperature.

**Structural properties of radiolytic electrode.** Scanning electron microscopy (SEM) images and X-ray diffraction (XRD) data for the nanoporous  $\text{TiO}_2$  are shown in Fig. 2. The cross-sectional SEM image shows the existence of nanopores 100 nm in diameter and 1  $\mu\text{m}$  deep with a spacing of 100 nm (Fig. 2a). Figure 2b shows a top-view SEM image of a 50-nm-thick Pt film coated surface of nanoporous  $\text{TiO}_2$ . After Pt deposition on nanoporous  $\text{TiO}_2$  film, the size of Pt nanoholes turns out to be approximately 10 ~ 20 nm

(Fig. 2b, inset). The density of holes is  $3 \sim 5 \times 10^9 \text{ cm}^{-2}$ . As shown by the XRD data in Fig. 2c, after the as-deposited Ti was anodised for 5 min, the intensity of the Ti (002) peak decreased compared to that of the Ti (001) peak, indicating the presence of vertically arranged uniform nanopores along the  $\langle 002 \rangle$  direction of the Ti. After the anodised Ti was thermally oxidised at 450 °C for 2 hours, the (001) and (002) peaks of Ti disappeared, and a new peak (37.24°) corresponding to the rutile crystalline structure appeared, indicating that  $\text{TiO}_2$  has a band gap of 3.2 eV<sup>39</sup>.

**Electrical properties of radiolytic cell.** Illustrations and photographs of the test setup and of the Pt/nanoporous  $\text{TiO}_2$  cathode are shown in Figs. 3a and b, respectively. During our experiment, gas bubbles on the PET plastic shielding film of the Sr-90/Y-90 source (Fig. 3a) clearly demonstrated the occurrence of water splitting. To evaluate the radiolytic performance of the Pt/nanoporous  $\text{TiO}_2$  electrode in a 1 M KOH aqueous solution, we employed a potentiostat. We measured the current density-voltage characteristics (Fig. 3c), open circuit voltage and the current density at 0 V, -0.1 V, -0.4 V, -0.7 V, and -0.9 V for 1200 seconds each under continuous irradiation (Fig. S2). Figure 3c shows the current density - voltage ( $J$ - $V$ ) characteristics for the Pt/nanoporous  $\text{TiO}_2$  radiolytic electrode (red line) under irradiation. For comparison, we measured the radio current of a nanoporous  $\text{TiO}_2$  electrode (blue line) under irradiation and the dark current of Pt/nanoporous  $\text{TiO}_2$  (black line) under no irradiation. While the radio current of nanoporous  $\text{TiO}_2$  is slightly larger than the dark current of Pt/nanoporous  $\text{TiO}_2$ , the radio current of Pt/nanoporous  $\text{TiO}_2$  is significantly larger than both the radio current of nanoporous  $\text{TiO}_2$  and the dark current of Pt/nanoporous  $\text{TiO}_2$ . The radio current density of Pt/nanoporous  $\text{TiO}_2$  is saturated at  $-175.4 \mu\text{A}/\text{cm}^2$  for 0 V, while the dark current density of Pt/nanoporous  $\text{TiO}_2$  and the radio current density of  $\text{TiO}_2$  are approximately  $-1.051 \mu\text{A}/\text{cm}^2$  and  $-0.0719 \mu\text{A}/\text{cm}^2$ , respectively. At -0.9 V, the radio current density of Pt/nanoporous  $\text{TiO}_2$ , the dark-current density of Pt/nanoporous  $\text{TiO}_2$ , and the radio current density of  $\text{TiO}_2$  are  $-83.336 \mu\text{A}/\text{cm}^2$ ,  $70.31 \mu\text{A}/\text{cm}^2$ , and  $2.85 \mu\text{A}/\text{cm}^2$ , respectively. These measurement data are summarized and reshaped into Table S1 to compare the performance of the irradiated devices with Pt/nanoporous  $\text{TiO}_2$  and nanoporous  $\text{TiO}_2$ . Figure 3d manifests the clear difference in output power from devices with and without the plasmonic Pt layer. The output power densities ( $11.59 \mu\text{W}/\text{cm}^2$  at -0.1 V and  $75.02 \mu\text{W}/\text{cm}^2$  at -0.9 V) of the Pt/nanoporous  $\text{TiO}_2$  electrode are higher than the power densities ( $-0.0027 \mu\text{W}/\text{cm}^2$  at

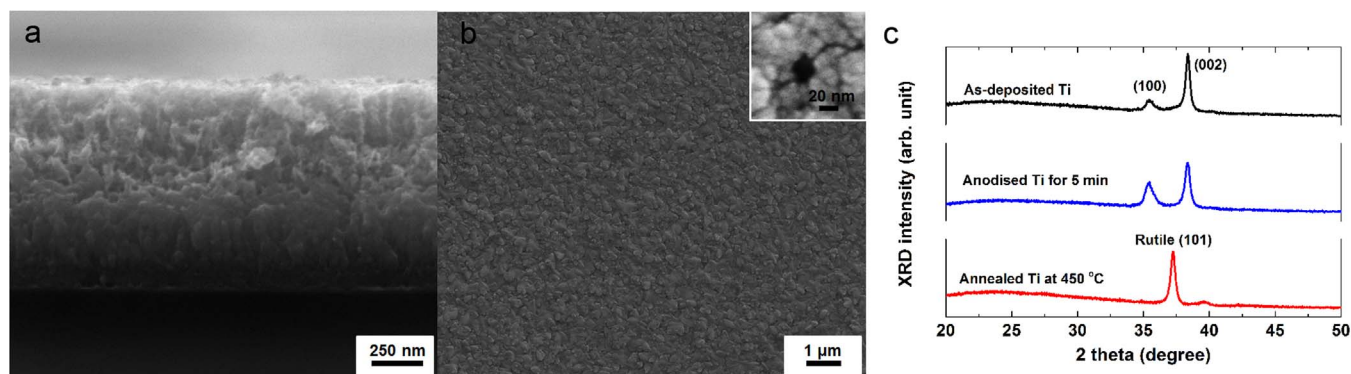


**Figure 2 | Radiolytic electrode.** (a), Cross-sectional SEM image of nanoporous TiO<sub>2</sub> on glass. (b), SEM image of Pt-coated nanoporous TiO<sub>2</sub> viewed from the top and the inset is a SEM image of a nanohole. (c), XRD data of as-deposited Ti (black line), anodised Ti (blue line), and rutile TiO<sub>2</sub> (red line).

−0.1 V and −2.565 μW/cm<sup>2</sup> at −0.9 V) of nanoporous TiO<sub>2</sub>. For a radioactive material activity of 15 mCi (±10%), the total number of beta particles per unit time is estimated to be  $5.55 \times 10^8 \text{ s}^{-1}$ , and the total input power density of the beta particles is 139.238 μW/cm<sup>2</sup>, when the average kinetic energy of Sr-90/Y-90 is 490.96 keV. From this data, maximum energy conversion efficiency ( $\eta$ ) of our device was approximately estimated to be 53.88% at −0.9 V using  $\eta = \frac{P_{chem}}{P_{rad}} \cdot \frac{P_{out}}{P_{chem}}$ , where  $P_{rad}$ ,  $P_{chem}$ , and  $P_{out}$  are radiation power density of source (139.238 μW/cm<sup>2</sup>), chemical power density in water, and, output power density of device (75.02 μW/cm<sup>2</sup>), respectively. One possible reason for the high output power density under irradiation is that a certain level of the EHP ionisation energy of beta particles can easily excite electrons because the EHP ionisation energy is much higher than the band gap of each material while a large portion of the spectrum of solar light is below the TiO<sub>2</sub> band gap, indicating that the TiO<sub>2</sub> layer does not absorb sunlight well. Therefore, beta particles are a reliable energy source for electricity generation via water splitting.

**Energy absorption of electron beam in the radiolytic cell using numerical simulation.** To study the mechanism of the enhanced power conversion of beta radiation, we calculated the energy absorbed in an aqueous solution using Monte Carlo (MC) simulations<sup>40</sup>. The number of electrons utilised in this simulation was 10,000, and the kinetic energy of the electron beam was 546 keV. A beta particle is an electron,  $e^-$ , or a positron,  $e^+$ , that is generated when the neutron to proton ratio in the nucleus is too large, making the nucleus unstable<sup>41</sup>. In this simulation, the presence of secondary electrons generated by primary electrons was ignored, and the electron beam was defined by a Gaussian distribution. The energy absorbed by the TiO<sub>2</sub> film was calculated to be approximately 0.25% of the total energy of the electron beam (Fig. 4). In the middle of the water, the absorbed energy was approximately 55.57%. Note that the incident beta radiation can be scattered and reflected by our nanoporous structure, indicating that more energy will be absorbed by Pt/nanoporous TiO<sub>2</sub> and water than expected in this simulation. Beta radiation can create vacancies in solids by primary knock-on atoms (PKA). For rutile TiO<sub>2</sub>, the threshold displacement energy is about 47 eV<sup>42</sup>. A required incident kinetic energy level of beta radiation for the vacancy production can be estimated from the displacement energy equation,  $T_m = 2(E + 2mc^2)E/Mc^2$ , where  $E$  is kinetic energy of beta radiation and  $c$  is speed of light.  $m$  and  $M$  are masses of electron and target atom, respectively. Figure S3 shows the relationship between the incident kinetic energy of beta radiation and the threshold displacement energy. Under beta radiation, the threshold displacement energy of 47 eV is equivalent to the incident kinetic energy of 271 keV for oxygen and 633.5 keV for

titanium as shown in Fig. S3. We also found from MC simulations that the water can absorb beta radiation of 356 keV. Because the PKA damage in TiO<sub>2</sub> occurs from the kinetic energy over 271 keV as shown in Fig. S3, the performance degradation of our radiolytic cell might begin with the kinetic energy over 627 keV. Although beta radiation from Sr-90/Y-90 includes higher energy beta particles than 627 keV as shown in Fig. S4, our radiolytic cell didn't show any performance degradation for about 6 hours (Fig. S2). Moreover, water can absorb 72.02% of the total kinetic energy in emission spectrum of Sr-90/Y-90. To determine the total kinetic energy passing through Pt/nanoporous TiO<sub>2</sub>, we considered the directional loss of radiation source. As shown in Fig. S5, the directional loss of our radiolytic cell is estimated to be approximately 54.88% and the amount of kinetic energy higher than 627 keV is only 12.62% of the total kinetic energy of beta radiation, indicating that performance degradation of our radiolytic cell may not be serious. Here, incident high-energy beta particles can excite electrons in the semiconductor via their energy loss, which is defined as the electron-hole pair (EHP) ionisation energy given by  $W_{\pm} \approx 2.8E_g + E_{ph}$ , where  $E_g$  and  $E_{ph}$  are the band gap and phonon energies ( $0.5 \leq E_{ph} \leq 1 \text{ eV}$ ), respectively<sup>43</sup>. For TiO<sub>2</sub>,  $W_{\pm}$  is approximately 9.46 eV. Because the high EHP ionisation energy is sufficient for tunnelling through a low Schottky barrier at the TiO<sub>2</sub>/liquid interface, the radio current of nanoporous TiO<sub>2</sub> is lower than the radio current of Pt/nanoporous TiO<sub>2</sub>, as shown in Fig. 3c. When beta particles pass through the TiO<sub>2</sub> layer (1 μm), the number of generated EHPs is estimated to be approximately 144 per single beta particle, that is, the deposition power is estimated to be 0.12 μW/cm<sup>2</sup>. Although most of the EHPs generated within the depletion region are separated due to the built-in potential of the thin TiO<sub>2</sub> layer, the measured output power density was much less than the expected values of 75.02 μW/cm<sup>2</sup> at −0.9 V. This result indicates that the EHPs generated in TiO<sub>2</sub> via beta radiation are not sufficient to produce the total output power density measured in the experiment.

### Generation and behaviour of free radicals under beta radiation.

To understand the highly enhanced output power, it is necessary to understand the details of water radiolysis. High-energy electrons passing through an aqueous solution can ionise or excite water molecules, forming a number of transition species and stable products, as shown by the equation  $\text{H}_2\text{O} \xrightarrow{\text{ionising radiation}} e_{aq}^-, \cdot\text{OH}, \text{H}^{\cdot}, \text{HO}_2^{\cdot}, \text{H}_3\text{O}^+, \text{OH}^-, \text{H}_2\text{O}_2, \text{H}_2^{\cdot}$ . High levels of these products are formed by the absorption of 100 eV in the medium. The generated radicals are powerful redox reagents, i.e.,  $e_{aq}^-$  is a strong reducing agent,  $\text{H}^{\cdot}$  is an equally strong reducing and oxidising agent, and  $\cdot\text{OH}$  is a powerful oxidising agent. In water at high pH,  $e_{aq}^-$  and  $\cdot\text{OH}$  are produced in the largest quantities by the beta radiation. The

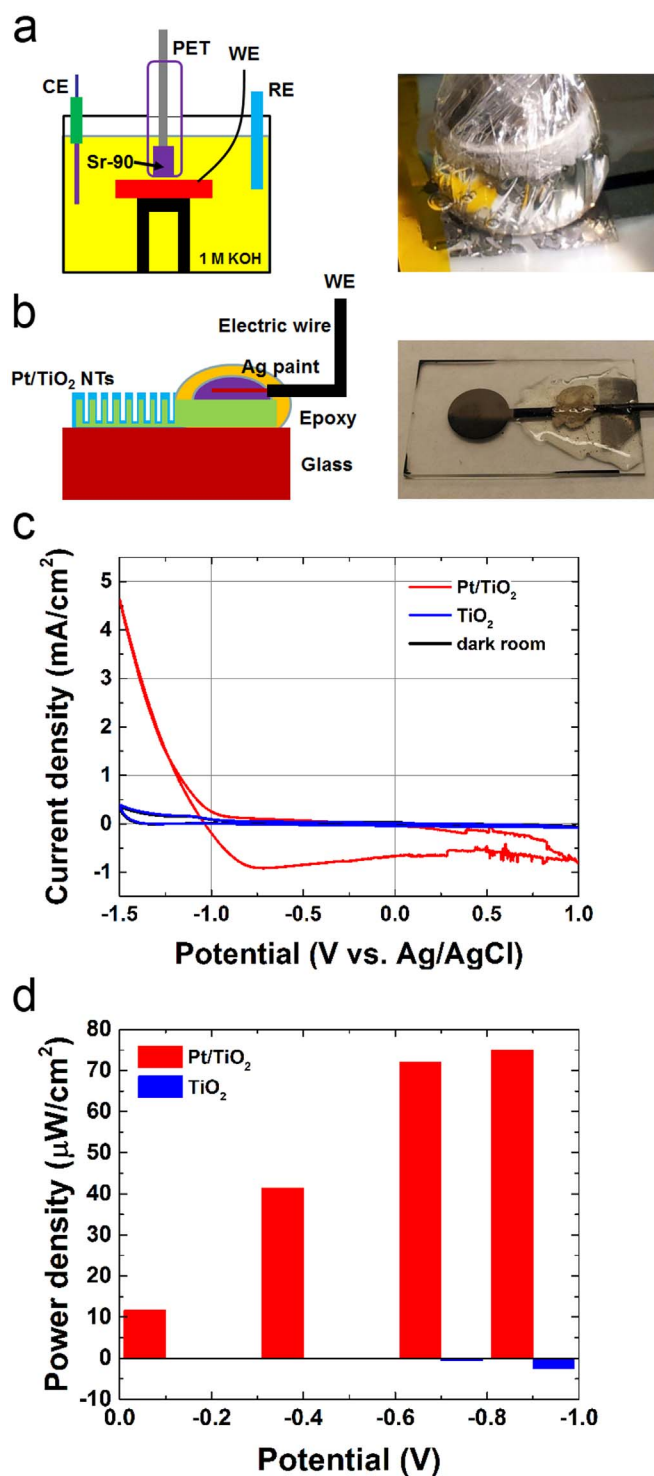


**Figure 3 | Radio-current output at the Pt/nanoporous TiO<sub>2</sub> electrode.** (a), Schematic view of the testing setup for Pt/nanoporous TiO<sub>2</sub> under irradiation and a photograph of the Sr-90/Y-90 source with gas bubbles attached to the outer surface of the PET film. (b), Schematic diagram and photograph of the Pt/nanoporous TiO<sub>2</sub> electrode. (c), *J-V* characteristics of irradiated devices with Pt/nanoporous TiO<sub>2</sub> (red line) and nanoporous TiO<sub>2</sub> (blue line) radiolytic electrodes and of unirradiated device with Pt/nanoporous TiO<sub>2</sub> (black line) in a dark room. (d), Power densities of irradiated devices with Pt/nanoporous TiO<sub>2</sub> (red bar) and nanoporous TiO<sub>2</sub> (blue bar). The area of the electrode is 1 cm<sup>2</sup>.

standard potentials of  $e_{aq}^-$  and  $\cdot\text{OH}$  are  $E^0(\text{H}_2\text{O}/e_{aq}^-) = -2.9 \text{ V}_{\text{NHE}}$  and  $E^0(\cdot\text{OH}/\text{H}_2\text{O}) = +2.7 \text{ V}_{\text{NHE}}$ , respectively<sup>45</sup>. These two species ( $e_{aq}^-$  and  $\cdot\text{OH}$ ) react with water molecules during water radiolysis and then remain in the aqueous solution. They can then no longer react with each other or with surrounding water molecules. Once these two species ( $e_{aq}^-$  and  $\cdot\text{OH}$ ) are solvated in an aqueous solution,

they can be surrounded by water molecules in a meta-stable state for a few  $\mu\text{s}$ <sup>45,46</sup>. It is well known that water has a very large dielectric constant and consists of polar molecules, which prevent the electrostatic attraction between positive and negative charges and maintain the separated state of charges surrounded by oppositely charged ends of water dipoles. During the long lifetime of solvated

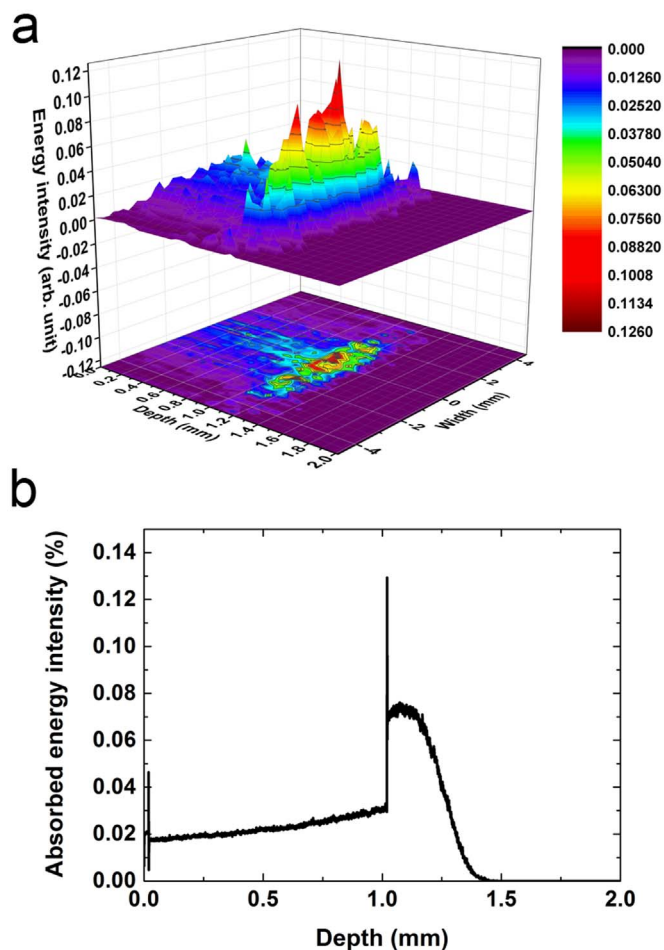


**Figure 4** | MC simulation of the electron beam in the radiochemical cell. (a), Absorbed energy distribution of the electron beam in the PET (20  $\mu\text{m}$ )/water (1 mm)/Pt (50 nm)/TiO<sub>2</sub> (1  $\mu\text{m}$ )/glass (1 mm) structure. (b), Cross-sectional view of the absorbed energy intensity at the centre of the electron irradiation.

electrons, beta radiation will continuously increase the number of solvated electrons in the water until they finally move to the surface of the water, where they are emitted as thermal energy. The floated electrons form the negatively charged surface of water<sup>47</sup>. Theoretically, water has lower standard potential ( $E^0(\text{H}_2\text{O}/\text{O}_2) = +0.82 \text{ V}_{\text{NHE}}$  and  $E^0(\text{H}_2\text{O}/\text{H}_2) = -0.41 \text{ V}_{\text{NHE}}$ ) than free radicals, indicating that electrochemical energy of water is lower than that of free radicals. It was also reported that high electrochemical energy of solvated electrons ( $e_{\text{aq}}^-$ ) can enable difficult chemical reactions to happen<sup>48</sup>. Moreover, the presence of an external electric field or electromagnetic field can release the solvated electrons from their confined environment of surrounding molecules<sup>49</sup>. This is because  $e_{\text{aq}}^-$  in water has very small diffusion efficiency ( $4.8 \times 10^{-5} \text{ cm}^2/\text{s}$ ) and electron mobility ( $1.84 \times 10^{-3} \text{ cm}^2/\text{V}\cdot\text{s}$ )<sup>50</sup>. Solvated electrons in water also need to get over the potential barrier of 0.2 ~ 0.5 eV set by the surrounding rigid water molecule network. Moreover, because water is located between both Pt electrodes (plasmonic layer and counter electrode), if same electrochemical reactions occur on both Pt surfaces, simply no current flow is expected.

**FDTD simulations of Pt/nanoporous TiO<sub>2</sub> on glass under an e-beam irradiation of 546 keV and optical measurement.** One available external electric field in our device is the localised electric fields from the surface plasmons of the Pt nanoholes. To generate surface plasmons on the Pt/nanoporous TiO<sub>2</sub> radiolytic electrode, we

performed 3D-FDTD (finite-difference time-domain) numerical simulations using a commercially available FDTD code for simulating electron irradiation<sup>51</sup>. In FDTD, the macroscopic Maxwell equations are solved in discretised space and time to follow the response of a material to an applied electric field. For a numerical investigation of the beta radiation-excited photon emission in Pt/nanoporous TiO<sub>2</sub>, the electron beam can be modelled as a line current density source represented by  $\vec{J}(t, \vec{r}) = -ev\hat{u}_z\delta(z-vt)\delta(x-x_0)\delta(y-y_0)$ , where  $e$  is the electronic charge,  $v$  is the electron velocity,  $(x_0, y_0)$  represents the position of the focused electron beam,  $z$  is the direction of the electron velocity, and  $\hat{u}_z$  is the unit vector along the  $z$  direction. In the simulation, the current density was modelled as a series of dipoles with a temporal phase delay ( $z/v$ ) related to the electron velocity,  $v$  (in this simulation,  $v = 0.875c$ , corresponding to the beta particle's kinetic energy of 546 keV used in the experiment, and  $c$  is the velocity of light in free space). We conducted our simulations for three different points denoted 1–3 in the middle of a pore, at the side wall of a pore, and between two pores, as depicted in Fig. 5a.

To simulate the near-field electric intensities and emission spectra at the different positions, the induced electric field distributions were calculated by  $[E]^2/[E_0]^2$ , where  $E$  and  $E_0$  are the generated and minimum electric field intensities, respectively, emitted normal and parallel to the Pt surface in the wavelength range of 200 to 700 nm. We investigated the near-field intensity distributions on Pt/nanoporous TiO<sub>2</sub> at the different positions under focused electron irradiation using FDTD simulations. As shown in Fig. 5b, the highest emitted spectral peaks were calculated to occur at wavelengths of 293 nm, 517 nm, and 376 nm when the electron irradiation is focused near positions 1, 2, and 3, respectively. These results indicate that the strongest surface plasmon energy (4.23 eV) and field intensity are generated when the nanohole is irradiated. Such strong surface plasmons have been observed in Pt nanostructures at similar energy levels due to an interband transition of the particles<sup>52–54</sup>. The diffraction pattern is also shown for position 3 on periodic Pt/nanoporous TiO<sub>2</sub>. To confirm the surface plasmons, we measured the reflectance of Pt/nanoporous TiO<sub>2</sub> structures using an UV-VIS spectrometer. As shown in Fig. 5b, marks 1–3 are the calculated emission spectra of Pt/nanoporous TiO<sub>2</sub> in water, while mark 4 is the measured reflectance of Pt/nanoporous TiO<sub>2</sub> in air. The reflection peaks (colour dots) of mark 4 were found at the similar positions with respect to the simulated emission peaks shown at marks 1–3. The strongest reflection peak (purple arrow) of Pt/nanoporous TiO<sub>2</sub> is shown at 245 nm (5.06 eV) by plasmon resonant coupling in air/Pt nanoholes. To understand the surface plasmon phenomena between two materials, we have to solve Maxwell's equation for the electromagnetic wave at the interface between two materials, which has relative dielectric functions  $\epsilon_1 (= \epsilon'_1 + i\epsilon''_1 = (n_1^2 - \kappa_1^2) + i(2n_1\kappa_1))$  and  $\epsilon_2 (= \epsilon'_2 + i\epsilon''_2 = (n_2^2 - \kappa_2^2) + i(2n_2\kappa_2))$  with the appropriated continuity relationship. Real and imaginary parts of the dielectric function are presented. The  $n_j$  and  $\kappa_j$  are refractive index and extinction coefficient, respectively, and  $j$  is 1 or 2. By boundary conditions, the dispersion relation for a wave propagating on the surface is  $\omega = (ck)^2(\frac{1}{\epsilon_1} + \frac{1}{\epsilon_2})$ , where  $k (=k' + ik'')$ ,  $\omega$  and  $c$  are the wave number and the frequency of the wave, the speed of light, respectively<sup>55</sup>. For  $k'$  not to be purely imaginary,  $\epsilon'_1 = (n_1^2 - \kappa_1^2) < 0$  and  $|\epsilon'_1| > \epsilon'_2 = (n_2^2 - \kappa_2^2)$ . Based on this relationship, we have plotted a graph shown in Fig. S7. Since the surface plasmon energy occurs around  $|\epsilon'_1| \approx \epsilon'_2$ , the surface plasmon wavelengths can be found from crossing points on the Pt line (black line). Compared to the water/Pt (green/black) interface, the air/Pt (blue/black) interface shows the surface plasmon phenomena at a slightly shorter wavelength. These wavelengths at the crossing points (red and green dots) of water/Pt and air/Pt in Fig. S7 are very close to the wavelengths at the strongest reflection peaks (red and green dots) as marked 1 and 4

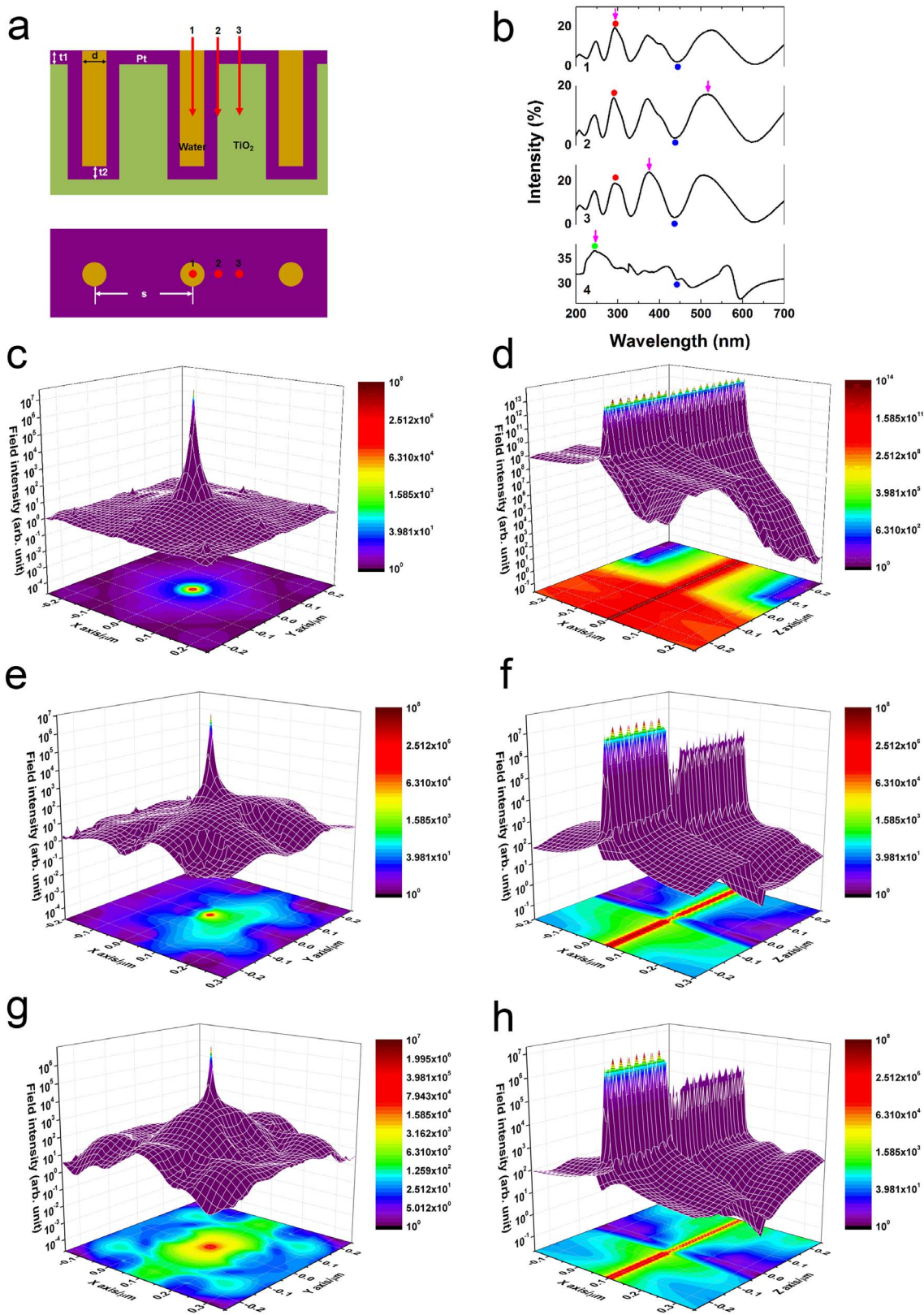


**Figure 5** | FDTD simulations of Pt/nanoporous TiO<sub>2</sub> on glass under an e-beam irradiation of 546 keV and optical measurement. (a), Cross-sectional view and top view for different e-beam positions marked as 1–3. In this simulation,  $d$ ,  $s$ ,  $t_1$ , and  $t_2$  are 10 nm, 200 nm, 50 nm, and 45 nm, respectively. (b), Emission spectra of the Pt/nanoporous TiO<sub>2</sub> surfaces at positions 1–3. Arrows indicate the highest peak positions. Mark 4 shows the reflection of Pt/nanoporous TiO<sub>2</sub> using an UV-VIS spectrometer. The same coloured dots indicate corresponding peaks of each spectrum. (c–d), Top and cross-sectional views of the near-field intensity distributions on Pt/nanoporous TiO<sub>2</sub> at the top level of Pt nanohole at mark 1 for 290 nm. (e–f), Top and cross-sectional views of the near-field intensity distributions on Pt/nanoporous TiO<sub>2</sub> at the top level of Pt nanohole at mark 2 for 287 nm. (g–h), Top and cross-sectional views of the near-field intensity distributions on Pt/nanoporous TiO<sub>2</sub> at the top level of Pt nanohole at mark 3 for 377 nm. The field intensity is shown on a log scale,  $[E]^2/[E_0]^2$ , where  $E$  and  $E_0$  are the generated and minimum electric field intensities, respectively.



in Figure 5b. Furthermore, the surface plasmon energy at the Pt/TiO<sub>2</sub> interface is consistent with a dip (blue dot) near 450 nm. Therefore, matched data from the emission peak shown at mark 4 in Fig. 5b and the green dot shown in Fig. S7 indicate evidence of plasmon resonant coupling in air/Pt nanoholes under e-beam irradiation. There are only very small amounts of variation among the two layer calculation data (Fig. S7), the multi layer simulation results (Fig. 5b-1 ~ 3) and the experimental data (Fig. 5b-4). In addition, as shown in the electron profiles in Figs. 5c–h, the highest electric field intensities can trace electron irradiation paths (electric dipoles), and simultaneously, the electric field intensities in the Pt/nanoporous TiO<sub>2</sub> structures are also strengthened near the electron irradiation paths by surface plasmons generated at the Pt nanoholes.

## Discussion

Electrons and holes that migrate to the surface of metal electrodes can reduce and oxidize the reactants adsorbed on the metal surfaces, respectively. The reduction (Red) and oxidation (Ox) reactions can produce the reduction current and oxidation current as shown in the *J-V* measurement data in Fig. 3c. The oxidation current density (lower red curve) is less than reduction current (upper red curve) at 0 V under irradiation, meaning that the reaction Red ⇒ Ox +  $ne^-$  is dominant on Pt/nanoporous TiO<sub>2</sub> and available electrons are provided continuously, whereas the current density data (upper and lower black lines) of unirradiated devices seem not much different. When the strongly localised electric field oscillates across the Pt surface, as illustrated in Figs. 5c–h, the displacement of the electron density in the Pt surface by the electric field oscillation generates a Coulombic attraction force that can interact with environmental molecular ions, meaning that the  $e_{aq}^-$  and  $^{\bullet}OH$  ions surrounded by water molecules can escape and attach to the Pt surface via localised surface plasmons. However, when the localised surface plasmon energy is less than the energy barrier of  $e_{aq}^-$  and  $^{\bullet}OH$ , they cannot coherently oscillate or escape from their meta-stable state. With respect to the vacuum level, the work functions of  $e_{aq}^-$  and  $^{\bullet}OH$  were calculated to be 1.6 eV and 7.2 eV, respectively, at pH 0. From the FDTD simulations, we obtained surface plasmon energy of 4.23 eV, which is 1.42 eV from the vacuum level and is higher than the energy level of  $e_{aq}^-$ , enabling electrons to escape from their meta-stable state and the escaped electrons to generate surface plasmons on the metal surface<sup>56,57</sup>. In addition, the presence of excited electrons indicates that excited holes with the same amount of energy (10.64 eV with respect to the vacuum level) exist. These excited holes can interact with  $^{\bullet}OH$  on the surface of Pt. The same phenomenon is responsible for Förster resonant energy transfer (FRET), in which an excited donor transfers energy to an acceptor group through a non-radiative process<sup>58</sup>. In fact, the Schottky junction of Pt/TiO<sub>2</sub> creates a space-charge region in the n-type TiO<sub>2</sub> layer because the electrons diffuse from the TiO<sub>2</sub> side to the Pt side whereas the holes move in the reverse direction. In the equilibrium state, an equal amount of electrons in Pt is trapped at the Pt/TiO<sub>2</sub> interface and builds up an internal electric field (0.45 eV) from the TiO<sub>2</sub> side toward the Pt side, preventing further movement of carriers. When surface plasmons are generated on Pt surface by beta radiation, electrons in Pt are pushed towards TiO<sub>2</sub> by the electric field created from surface plasmons, which is higher than the internal electric field, and holes move simultaneously towards the Pt/water surface interface. Accumulated holes can attract donors like negatively charged ions or radicals. Thus, the strong electric field enhancement can significantly increase the number of accumulated holes at the Pt/water interface and create a large internal potential difference. With the energy higher than the potential barrier (0.2 ~ 0.5 eV) of surrounding water molecules, solvated electrons ( $e_{aq}^-$ ) can be attracted toward the Pt surface rapidly in water. Moreover, surface plasmons have a resonance frequency of a few hundred of GHz in visible wavelength. This means that strong Coulombic attraction force oscillates very fast to attract

$e_{aq}^-$  in water. When the distance between the TiO<sub>2</sub> and Pt counter electrode is 5 cm, the electric field is approximately 0.09 V/cm and the speed of electrons in water reaches  $1.6256 \times 10^{-4}$  cm/s. If  $e_{aq}^-$  in water is 1 mm away from TiO<sub>2</sub>, it can move to the TiO<sub>2</sub> surface in 603 s and most solvated electrons will not arrive quickly at the TiO<sub>2</sub> electrode. Thus, as shown in Fig. S2, a slowly saturated curve of open circuit voltage is observed on TiO<sub>2</sub> electrode under beta radiation, while the Pt/TiO<sub>2</sub> electrode has a very fast saturated curve. The electric field of the TiO<sub>2</sub> electrode is much weaker than that of the Pt/TiO<sub>2</sub> electrode producing the surface plasmon effect, and the difference in electric field intensity may affect the collection of  $e_{aq}^-$  in water. Once  $e_{aq}^-$  is arrived at the electrode surface,  $e_{aq}^-$  is injected without any energy loss because the electrochemical energy is higher than the conduction band edge ( $-0.1 \sim -0.2 V_{NHE}$ ) of TiO<sub>2</sub>.

In principle, photovoltaic devices, such as dye-sensitised solar cells and photochemical cells, use the similar mechanism, but sunlight produces very few free radicals because it is composed of photon energies that lie primarily in the visible range (380 nm–780 nm). Differently, beta radiation many free radicals through the loss of kinetic energy in water. Then, the generation of localised surface plasmons on the Pt surface by beta radiation can enhance the chemical reactions involving free radicals produced by beta radiation in water. The reflection peak of Pt/nanoporous TiO<sub>2</sub> at 5.04 eV, and the similarity between the simulated emission spectra and measured reflection spectrum show that the surface plasmon resonance occurs at higher energy than the band gap energy of TiO<sub>2</sub>, indicating resonant energy transfer between TiO<sub>2</sub> and surface plasmons<sup>59–61</sup>. Because the increased population of hot electrons generated by surface plasmons decreases the thickness of the Pt/TiO<sub>2</sub> junction and increases its junction electric field<sup>62,63</sup>, the narrow junction enables carriers obtained from free radicals to efficiently move toward the contact metals without carrier relaxation in the thin film. We confirmed that significantly more power from the device with the plasmonic Pt layer was produced than that from the device without the plasmonic Pt layer. As shown in Fig. S12, increased surface plasmon energy can effectively transport hot carriers generated on a Pt surface. Therefore, we can conclude that the high power density obtained from our radiolytic cell may be attributed to the conversion of continuously generated free radicals with large electrochemical energy into electricity by the surface plasmon energy generated at the Pt surface. This finding reveals new mechanisms for power generation in radiolytic chemical cells. Our unique approach further paves the way for producing chemical cells with higher power density.

## Methods

**Sample preparation.** A 2- $\mu$ m-thick titanium film was deposited on a glass substrate using an RF sputtering system, and an area of 1 cm<sup>2</sup> was patterned for an electrode. The substrate was cleaned with a standard solvent cleaning process, dried under a flow of N<sub>2</sub> gas, and immediately anodised in a 0.01 wt% HF aqueous solution under an applied voltage of 40 V for 5 min. Immediately after cleaning and drying the anodised Ti films, the substrate was annealed in a convection oven at 450 °C for 2 hours. A 50-nm-thick Pt film was deposited on the thermally oxidised Ti films using an RF sputtering system. A copper wire was connected to the electrode of each sample and covered with epoxy to electrically isolate the electrolyte.

**Structural and optical properties.** Scanning electron microscopy (SEM) was performed using an FEI Quanta 600 FEG extended vacuum scanning electron microscope with an accelerating voltage of 10 kV and an energy dispersive spectrometer (Noran System Six). X-ray diffraction (XRD) analysis was conducted using a Rigaku Miniflex 600 X-ray diffractometer with Cu K $\alpha$  radiation. The reflection spectrum was measured using a Perkin-Elmer lambda 25 UV-VIS spectrometer and variable-angle reflectance accessory.

**Electrical properties.** Consecutive *J-V* measurements were collected from 1.0 V to  $-1.5$  V with respect to Ag/AgCl reference electrodes in a three-electrode system at a fixed scan rate of 0.05 V/s. The electrolyte solution was 1 M KOH (Sigma Aldrich, 99%). A radioisotope source (Sr-90/Y-90, 15 mCi) sealed in stainless steel was chosen for our experiment. The distance between the electrode and the radiation source required to maintain a constant activity of 15 mCi at the surface of the device was determined to be approximately 1 mm. A potentiostat (DY2322, Digi-Ivy) was



connected to the three (reference, counter, and working) electrodes for data collection. All experiments were performed in a dark room to eliminate the effects of a photocurrent. In addition, to ensure that the reaction only involved diffused radicals, the solution was not agitated.

**FDTD simulation.** We used Pt (50 nm)/nanoporous TiO<sub>2</sub> (1 μm) composed of a periodic array of nanoholes with a diameter of 10 nm and a depth of 505 nm. The electron beam was modelled as a series of closely spaced dipoles with a temporal phase delay defined by the velocity of the electron beam. In the absence of a structure, an electron beam moving at a constant velocity does not generate any radiation. The material properties used in the calculation are based on the dispersion data given in refs. 64 and 65. The detailed electron irradiation profiles at the different positions at the bottom level of the nanoholes in the supplementary information show the strong influence of the Pt/nanoporous TiO<sub>2</sub> structures on the scattering direction.

- Love, C. J. *Handbook of Cardiac Pacing*. (Landes Bioscience, Austin, 1999).
- Singh, N. *Radioisotopes-Applications in physical sciences*. (InTech inc, Rijeka, 2011).
- Corliss, W. R. & Harvey, D. G. *Radioisotopic power generation*. (Prentice-Hall, Englewood Cliffs, 1964).
- Bower, K. E., Barbanell, Y. A., Shreter, Y. G. & Bohnert, G. W. *Polymers, Phosphors, and Voltaics for Radioisotope Microbatteries*. (CRC Press, Boca Raton, 2002).
- Pfann, W. G. & Van Roosbroeck, W. Radioactive and photoelectric p-n junction power sources. *J. Appl. Phys.* **25**, 1422 (1954).
- Rappaport, P. The electron-voltaic effect in pn junctions induced by beta particle bombardment. *Phys. Rev.* **93**, 246–247 (1954).
- Olsen, L. C., Cabauy, P. & Elkind, B. J. Betavoltaic power sources. *Phys. Today* **65**, 35–38 (2012).
- Ko, W. & Hyneczek, J. Implant evaluation of a nuclear power source-Betacel® battery. *IEEE trans. on Biomed. Engr.* 238–241 (1974).
- Huffman, F. & Norman, J. Nuclear-fueled cardiac pacemakers. *Chest* **65**, 667–672 (1974).
- Wei, L. Parametric studies and optimization of the beta-voltaic cell--II open-circuit voltage and power efficiencies. *Solid-State Elec.* **18**, 71–77 (1975).
- Liu, B., Chen, K. P., Kherani, N. P. & Zukotynski, S. Power-scaling performance of a three-dimensional tritium betavoltaic diode. *Appl. Phys. Lett.* **95**, 233112 (2009).
- Eiting, C. J. *et al.* Demonstration of a radiation resistant, high efficiency SiC betavoltaic. *Appl. Phys. Lett.* **88**, 064101 (2006).
- Lu, M., Wang, G. & Yao, C. Gallium nitride for nuclear batteries. *Adv. Mater. Res.* **343–344**, 56–61 (2012).
- Sun, W. *et al.* A Three-Dimensional Porous Silicon p-n Diode for Betavoltaics and Photovoltaics. *Adv. Mater.* **17**, 1230–1233 (2005).
- Duggirala, R., Lal, A. & Radhakrishnan, S. *Radioisotope thin-film powered microsystems*. (Springer, New York, 2010).
- Wacharasindhu, T., Kwon, J. W., Meier, D. E. & Robertson, J. D. Radioisotope microbattery based on liquid semiconductor. *Appl. Phys. Lett.* **95**, 014103 (2009).
- Murray, R. *Nuclear energy* (Pergamon Press, Oxford, 1980).
- Collinson, E., Dainton, F. S. & Kroh, J. Effects of linear energy transfer of the radiolysis of water and heavy water. *Nature* **187**, 475–477 (1960).
- Khan, K. A. The radiation chemistry of water. *J. Chem. Soc. Pak* **3**, 105–110 (1981).
- Jonah, C. D. A short history of the radiation chemistry of water. *Rad. Res.* **144**, 141–147 (1995).
- Seino, S. *et al.* Enhancement of hydrogen evolution yield from water dispersing nanoparticles irradiated with gamma-ray. *J. Nucl. Sci. Technol.* **38**, 633–636 (2001).
- Cecal, Al *et al.* Use of some oxides in radiolytical decomposition of water. *Rad. Phys. Chem.* **62**, 333–336 (2001).
- Seino, S. *et al.* Hydrogen evolution from water dispersing nanoparticles irradiated with gamma-ray/size effect and dose rate effect. *Scripta Mater.* **44**, 1709–1712 (2001).
- Ershov, B. G. & Gordeev, A. V. A model for radiolysis of water and aqueous solution of H<sub>2</sub>, H<sub>2</sub>O, and O<sub>2</sub>. *Rad. Phys. Chem.* **77**, 928–935 (2008).
- Laverne, J. A. & Tandon, L. H<sub>2</sub> production in the radiolysis of water on UO<sub>2</sub> and other oxides. *J. Phys. Chem. B* **107**, 13623–13623 (2003).
- Wada, Y., Kawaguchi, K. & Myouchin, M. Decomposition of water and production of H<sub>2</sub> using semiconductor-photocatalytic effect induced by gamma ray from high radioactive waste. *Progress in Nuclear Energy* **29**, 251–256 (1995).
- Laverne, J. A. & Tonnie, S. E. H<sub>2</sub> production in the radiolysis of aqueous SiO<sub>2</sub> suspensions and slurries. *J. Phys. Chem. B* **107**, 7277–7280 (2003).
- Schierbaum, K. D. *et al.* The interaction of Pt with TiO<sub>2</sub>(110) surfaces: a comparative XPS, UPS, ISS, and ESD study. *Surf. Sci.* **345**, 261–173 (1996).
- Borodin, A. & Reichling, M. Characterizing TiO<sub>2</sub>(110) surface states by their work function. *Phys. Chem. Chem. Phys.* **12**, 15442–15447 (2011).
- Lide, D. R. *CRC Handbook of chemistry and physics* (CRC Press, Boca Raton, 2005).
- Heimann, D. Radiative decay of surface plasmons excited by fast electrons on periodically modulated silver surfaces. *J. Phys. C* **10**, 397–405 (1977).
- Bashevov, M. V., Jonsson, F., Krasavin, A. V. & Zheludev, N. I. Generation of traveling surface plasmon waves by free-electron impact. *Nano Lett.* **6**, 1113–1115 (2006).
- Cai, W. *et al.* Efficient generation of propagating plasmons by electron beams. *Nano Lett.* **9**, 1176–1181 (2009).
- Koh, A. L. *et al.* High-resolution mapping of electron-beam-excited plasmon modes in lithographically defined gold nanostructures. *Nano Lett.* **11**, 1323–1330 (2011).
- Das, P., Chini, T. K. & Pond, J. Probing higher order surface plasmon modes on individual truncated tetrahedral gold nanoparticle using cathodoluminescence imaging and spectroscopy combined with FDTD simulations. *J. Phys. Chem. C* **116**, 15610–15619 (2012).
- Petrik, N. G. & Kimmel, G. A. Electron-stimulated reactions in thin D<sub>2</sub>O films on Pt(111) mediated by electron trapping. *J. Chem. Phys.* **8**, 3727–3735 (2004).
- Koitaya, T., Nakamura, H. & Yamashita, K. First-principle calculations of solvated electrons at protic solvent-TiO<sub>2</sub> interfaces with oxygen vacancies. *J. Phys. Chem.* **113**, 7236–7245 (2009).
- Young, R. M. & Neumark, D. M. Dynamics of solvated electrons in clusters. *Chem. Rev.* **112**, 5553–5577 (2012).
- Buck, E. C. Effects of electron irradiation of rutile. *Radiat. Eff. Defect Solids* **133**, 141–152 (1995).
- Grimes, C. A. & Mor, G. K. *TiO<sub>2</sub> nanotube arrays: synthesis, properties, and applications*. (Springer, New York, 2009).
- Drouin, D. *et al.* CASINO V2.42: a fast and easy-to-use modeling tool for scanning electron microscopy and microanalysis users. *Scanning* **29**, 92–101 (2007).
- Lewis, E. E. *Fundamentals of nuclear reactor physics*. (Academic Press, London, 2008).
- Caër, S. L. Water radiolysis: influence of oxide surfaces on H<sub>2</sub> production under ionizing radiation. *Water* **3**, 235–253 (2011).
- Klein, C. A. Bandgap dependence and related features of radiation ionization energies in semiconductors. *J. Appl. Phys.* **39**, 2029–2038 (1968).
- Boag, J. W. & Hart, E. J. Absorption spectra in irradiated water and some solutions: absorption spectra of 'hydrated' electron. *Nature* **197**, 45–47 (1963).
- Keene, J. P. Absorption spectra in irradiated water and some solutions: optical absorptions in irradiated water. *Nature* **197**, 47–49 (1963).
- Avel, B. Hydrated interfacial ions and electrons. *Annu. Rev. Phys. Chem.* **64**, 533–552 (2013).
- Zhu, D., Zhang, L., Ruther, R. E. & Hamers, R. J. Photo-illuminated diamond as a solid-state source of solvated electrons in water for nitrogen reduction. *Nature Mater.* **12**, 836–841 (2013).
- Hase, H. & Higashimura, T. Trapped and solvated electrons produced in ethanol glass in the presence of an applied electric field. *J. Phys. Chem.* **83**, 822–823 (1979).
- Schmidt, K. H. & Buck, W. L. Mobility of the hydrated electron. *Science* **151**, 70–71 (1966).
- <http://www.lumerical.com>.
- Henglein, A., Ershov, B. G. & Malow, M. Absorption spectrum and some chemical reactions of colloidal platinum in aqueous solution. *J. Phys. Chem.* **99**, 14129–14136 (1995).
- Rivadulla, J. F. *et al.* Optical properties of platinum particles synthesized in microemulsions. *J. Phys. Chem. B* **101**, 8997–9004 (1997).
- Bassett, P. J. *et al.* Helium-I photoelectron spectra of tetrakis(trifluorophosphine)-nickel(0), -palladium(0), and -platinum(0). *J. Chem. Soc., Dalton Trans.* **21**, 2316–2319 (1974).
- Maier, S. A. *Plasmonics: Fundamentals and applications*. (Springer, New York, 2007).
- Atwater, H. A. & Polman, A. Plasmonics for improved photovoltaic devices. *Nature Materials* **9**, 205–213 (2010).
- Stratakis, E. & Kymakis, E. Nanoparticle-based plasmonic organic photovoltaic devices. *Materials Today* **16**, 133–146 (2013).
- Fadhali, M. *Advanced Photonic Sciences*. (Intech, Rijeka, 2012).
- Murakoshi, K. & Uosaki, K. Photon emission at metal/solution interface induced by electron injection from solvated electrons. *J. Vac. Sci. Technol. A* **10**, 2981–2984 (1992).
- Murakoshi, K. & Uosaki, K. Observation and mechanism of photon emission at metal-solution interfaces. *Phys. Rev. B* **47**, 2278–2288 (1993).
- Warren, S. C. & Thimsen, E. Plasmonic solar water splitting. *Energy Environ. Sci.* **5**, 5133–5146 (2012).
- Kempa, K. *et al.* Hot electron effect in nanoscopically thin photovoltaic junctions. *Appl. Phys. Lett.* **95**, 233121 (2009).
- Wang, F. & Melosh, N. A. Power-independent wavelength determination by hot carrier collection in metal-insulator-metal devices. *Nature Communications* **4**, 1711 (2013).
- Devore, J. R. Refractive indices of rutile and sphalerite. *J. Opt. Soc. Am.* **41**, 416–419 (1951).
- Palik, E. D. *Handbook of optical constants of solids*. (Academic Press, London, 1997).

## Acknowledgments

The authors are grateful for useful discussions for XPS analysis with Mr. Brian Porter and for TEM sample preparation with Ms. Jessica R. Terbush in the Material Research Center at the Missouri University of Science and Technology. The authors are also thankful for optical measurements and detailed discussions with Dr. Ping Yu at the University of Missouri.





## Author contributions

B.H.K. and J.W.K. performed the experiments, analysed the data, discussed the results and commented on the manuscript. J.W.K. conceived and supervised this study, and provided intellectual and technical guidance.

## Additional information

**Supplementary information** accompanies this paper at <http://www.nature.com/scientificreports>

**Competing financial interests:** The authors declare no competing financial interests.

**How to cite this article:** Kim, B.H. & Kwon, J.W. Plasmon-assisted radiolytic energy conversion in aqueous solutions. *Sci. Rep.* 4, 5249; DOI:10.1038/srep05249 (2014).



This work is licensed under a Creative Commons Attribution-NonCommercial-NoDerivs 4.0 International License. The images or other third party material in this article are included in the article's Creative Commons license, unless indicated otherwise in the credit line; if the material is not included under the Creative Commons license, users will need to obtain permission from the license holder in order to reproduce the material. To view a copy of this license, visit <http://creativecommons.org/licenses/by-nc-nd/4.0/>